Acta Geotechnica
DOI 10.1007/s11440-017-0534-4

RESEARCH PAPER

Localized failure in unsaturated soils under non-isothermal conditions

Xiaoyu Song[1] · **Kaiqi Wang**[1] · **Ming Ye**[2]

Received: 28 December 2016 / Accepted: 15 March 2017

Abstract Fluctuations of temperature and degree of saturation have considerable influence on the mechanical, hydraulic and retention properties of unsaturated soils. Localized failure is a ubiquitous feature of geomaterials. Major research on localized failure of geomaterials has been focused on geomaterials under the isothermal condition. In this article, we study the localized failure of unsaturated soils under non-isothermal conditions. In particular, we derive the isothermal and adiabatic bifurcation conditions from a homogeneous deformation at the constitutive level under a locally drained condition. A recently proposed meso-scale constitutive model for thermal unsaturated soils is used to derive the isothermal and adiabatic acoustic tensors. We present the spectral form of the consistent tangential elasto-plastic operator from a local material integration algorithm. The numerical simulations at the material level are conducted to study the impact of temperature on localized failure of unsaturated soils under the plane strain condition. The numerical results show that the timing and the critical angle of bifurcation are dependent on temperature.

Keywords Bifurcation · Localized failure · Plasticity · Temperature · Unsaturated soils

✉ Xiaoyu Song
xiaoyu.song@essie.ufl.edu

[1] Department of Civil and Coastal Engineering, University of Florida, Gainesville, FL 32611, USA

[2] Department of Scientific Computing, Florida State University, Tallahassee, FL 32306, USA

1 Introduction

Localized failure is a ubiquitous feature of geomaterials. The onset of shear banding may dramatically reduce the overall load carrying capacity as well as impact the transport properties of geomaterials. For these reasons, shear banding in saturated soils have been investigated theoretically, experimentally and numerically over the past several decades (e.g.,[16, 40, 43, 61, 62]). However, there is few research on the localized deformation of unsaturated soils. For instance, Borja [7] proposed a mathematical framework to detect the onset of strain localization in unsaturated soils at the constitutive level under the isothermal conditions. Ehlers et al. [20] investigated the inception of strain localization in partially saturated soils via a finite element model formulated based on the general porous media theory [14, 15]. Schiava and Etse [48] analyzed the condition for discontinuous bifurcation in unsaturated soils for different suctions and effective stress states. Callari et al. [13] studied the inception and propagation of strain localization in unsaturated soils via an enhanced finite element technique. Buscarnera and Nova [12] studied instabilities of unsaturated soils in triaxial testing via a second-order work concept. Peric et al. [39] presented general analytical solutions for the onset of strain localization in unsaturated soils. Recent research conducted by the first author showed that the material heterogeneities (i.e., density and degree of saturation) are potential triggers on localized failure in unsaturated soils [52–55, 57, 58].

The above study of strain localization in unsaturated soils has been focused on unsaturated soils at constant ambient temperature. However, in recent years the thermal–hydro-mechanical analysis of unsaturated soils has received increasing interest in the geomechanics community because of its wide spectrum of engineering

Published online: 11 April 2017

applications, for instance, geothermal structures [33], petroleum drilling, injection and production activities [18], and zones around high-voltage cables [2, 36]. This can be seen from the recent experimental work (e.g., [42, 46, 59]) and constitutive modeling (e.g., [5, 17, 21, 25, 35, 63]) of thermal unsaturated soils. On the experimental side, Salager et al. [46] investigated the influence of temperature and suction effects on compressibility and preconsolidation pressure of a sandy silt, and proposed an evolution equation for the apparent preconsolidation stress with respect to temperature and suction, which has been used in thermal constitutive models for unsaturated soils (e.g., [21, 56]). Recently Uchaipichat and Khalili [59] presented an experimental study on non-isothermal behavior of unsaturated soils under the triaxial condition.

On the constitutive modeling of thermal unsaturated soils, the first constitutive model was proposed by Gens [25]. This thermomechanical model is a combination of the constitutive model for unsaturated soils under the isothermal condition [1] and a thermoplastic modeling for saturated soils [29]. Wu et al. [63] proposed a thermohydro-mechanical constitutive model for unsaturated soils in which the effect of temperature on the water retention curve was considered explicitly. Bolzon and Schrefler [5] modified an elastic–plastic model for partially saturated soils to take into account the temperature effect. Francois and Laloui [21] presented a unified approach dealing with the thermoplasticity of saturated and unsaturated soils in a highly coupled framework. Dumont et al. [17] proposed a thermal–hydro-mechanical model for unsaturated soils based on a microstructural model for capillary stress. Masin and Khalili [35] formulated a thermomechanical model for unsaturated soils based on hypoplasticity. Recently the first author of this paper presented a meso-scale thermal constitutive model for unsaturated soils which can capture both the inherent and induced heterogeneity of porosity [56].

Another factor that needs to be considered in modeling unsaturated soils is water retention model [23, 60]. Water retention model is a relationship between water content and water potential in unsaturated porous media. It has been recognized that the water retention curve for unsaturated soils is dependent on the density of soils [44] as well as temperature [45, 47]. Experimental results showed that the retention curves shift toward lower saturations in the suction–saturation plot with increasing temperatures (see Fig. 1). The major reason for this observed phenomenon is the interfacial tension between the water and the grains decreases as temperature increases [41]. Grant and Salehzadeh [27] investigated the temperature effects on the capillary pressure and contact angle γ_A between water and solid phase, and proposed a temperature-dependent soil–water retention curve, which is a variant of the model

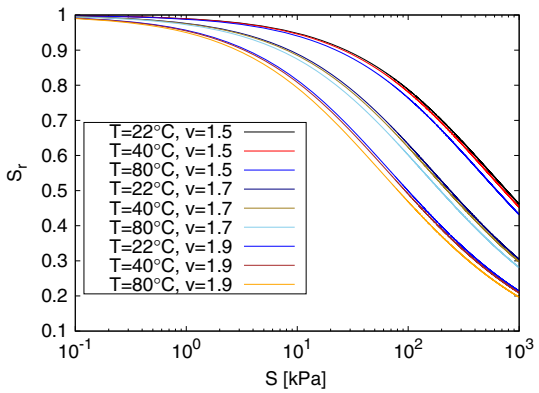

Fig. 1 Water retention *curves* for three different specific volumes at three different temperatures. *S* suction, *v* specific volume

proposed by van Genuchten [60]. However, none of the aforementioned water retention models considered the influence of the density of the solid phase on the water retention in porous media. Salager et al. [45] proposed a general law quantifying the variation of suction with water content, temperature and void ratio, which was validated by their own laboratory experiments. This law was adopted to describe soil–water retention in the meso-scale constitutive model for thermal unsaturated soils [56].

The inception of shear banding in geomaterials can be described as a bifurcation of the incremental solution for a boundary value problem. Mechanically, shear banding can be described as a strong (i.e., displacement) or weak (i.e., strain) discontinuity problem. In this article, we derive a bifurcation condition from a homogeneous deformation at the constitutive level under the fully "drained" condition. Here, the local fully "drained" condition means the pore pressures of water and air, and temperature inside and outside the shear band are continuous. The meso-scale constitutive model for thermal unsaturated soils is used to derive the "drained" acoustic tensor. We present the spectral form of the consistent tangent operator from a local material integration algorithm. The numerical simulations at the material point level are conducted to study the impact of the elevated constant temperature and temperature variations on localized failure in unsaturated soils under the suction-controlled plane strain condition. The numerical results show that the fluctuation of temperature may facilitate localized failure in unsaturated soils. We also present the detection of localized deformation under the different initial dry density of unsaturated soils that demonstrates that the impact of temperature on localized failure is sensitive to the initial dry density of unsaturated soils.

As for notations and symbols used in this article, bold-faced letters denote tensors and vectors; the symbol "." denotes an inner product of two vectors; the symbol ":" denotes an inner product of two second-order tensors, or

double contraction of adjacent indices of tensors of rank two or higher; the symbol "$\otimes$" denotes a juxtaposition. For any symmetric second-order tensors $\boldsymbol{\alpha}$ and $\boldsymbol{\beta}$, $(\boldsymbol{\alpha} \otimes \boldsymbol{\beta})_{ijkl} = \alpha_{ij}\beta_{kl}$.

2 A meso-scale thermal plasticity model for unsaturated soils

In the section, we briefly introduce the key elements of a meso-scale thermal constitutive model for unsaturated soils [56]. We first introduce the effective stress chosen for this constitutive model because the stress tensor is a key element to model unsaturated soils [26]. There are two types of stress tensors proposed to model unsaturated soils. In the first category the total stress is decomposed into a net stress (i.e., total stress minus pore air pressure) and suction (i.e., pore air pressure minus pore water pressure) (e.g., [1, 22]). For the second one the Bishop-type effective stress [3, 4] is used to model the solid phase via

$$\boldsymbol{\sigma}' = (\boldsymbol{\sigma} + p_a\mathbf{1}) - \chi(p_a - p_w)\mathbf{1}, \tag{1}$$

where $\boldsymbol{\sigma}$ and $\boldsymbol{\sigma}'$ are the total and effective Cauchy stress tensor respectively; p_a and p_w are pore air and pore water pressures, respectively; $\boldsymbol{I}$ is the second-order identity tensor respectively; χ is the effective stress parameter, which equals to 1 for saturated soils and zero for dry soils. Here we follow the convention in continuum mechanics (i.e., stress and strain in compression are negative and pore pressure in compression is positive). In general, to model partially saturated porous media, it is convenient to apply the Bishop effective stress to describe unsaturated soils though selection of which stress tensor mostly depends on the convenience [38]. The generalized Bishop effective stress transfers the multiphase, multistress sate porous material into a mechanically equivalent, single-phase, single-stress state material [31, 34, 37]. In this paper, we use the generalized Bishop-type effective stress [49] combined with thermal effect to describe the mechanical behavior of unsaturated soils,

$$\boldsymbol{\sigma}' = (\boldsymbol{\sigma} + p_a\mathbf{1}) - S_r(p_a - p_w)\mathbf{1}, \tag{2}$$

where χ is replaced by degree of saturation S_r. Furthermore, we assume that the total strain is decomposed into thermal elastic and thermal plastic parts under the assumption of the infinitesimal deformation.

$$\boldsymbol{\epsilon} = \boldsymbol{\epsilon}^e + \boldsymbol{\epsilon}^p. \tag{3}$$

Next, we briefly describe the main elements of this thermoplastic constitutive model for unsaturated soils.

2.1 Thermal elastic model

For the thermal elasticity, we assume that the temperature variation only impacts the volumetric strain of soils [29]. That is, the elastic region is determined by the isothermal elastic deformation and thermal volumetric expansion. In particular, the elastic modulus (i.e., bulk modulus and shear modulus) is assumed to be governed by the isotropic strain-energy function for modeling granular materials under the isothermal condition [10, 11],

$$\Psi(\epsilon_v^e, \epsilon_s^e) = \tilde{\Psi}(\epsilon_v^e) + \frac{3}{2}\mu^e(\epsilon_s^e)^2, \tag{4}$$

where

$$\tilde{\Psi}(\epsilon_v^e) = -p_0\tilde{\kappa}\exp\omega, \omega = -\frac{\epsilon_v^e - \epsilon_{v0}^e}{\tilde{\kappa}}, \mu^e = \mu_0 + \frac{\alpha}{\tilde{\kappa}}\tilde{\Psi}(\epsilon_v^e). \tag{5}$$

Here $\tilde{\kappa}$ is the elastic compressibility index; ϵ_{v0}^e is the elastic volumetric strain corresponding to a mean normal stress of p_0; μ^{e} is the elastic shear modulus, which contains a constant term μ_0 and a term that varies with the elastic volumetric strain through the constant coefficient α.

The independent variables are the isothermal infinitesimal volumetric strain and isothermal deviatoric strain,

$$\epsilon_v^e = \mathrm{tr}(\boldsymbol{\epsilon}^{\mathrm{e}}) - \epsilon_{\mathrm{T}}^{\mathrm{e}}, \epsilon_{\mathrm{s}}^{\mathrm{e}} = \sqrt{\frac{2}{3}}\|\boldsymbol{\epsilon}^{\mathrm{e}} - \frac{1}{3}\mathrm{tr}(\boldsymbol{\epsilon}^{\mathrm{e}})\boldsymbol{I}\|. \tag{6}$$

The thermal volumetric strain is determined by the following equation,

$$\epsilon_T^e = \beta_s(T - T_0), \tag{7}$$

where β_s is the volumetric thermal expansion coefficient of the solid skeleton; T is the soil temperature; T_0 is the reference temperature (ambient temperature). We use the following expression for β_{s0} [21] but assuming that β_{s0} is independent of the effective mean pressure and the initial critical state pressure,

$$\beta_s = \beta_{s0}\left(1 - \frac{T - T_0}{100}\right), \tag{8}$$

where β_{s0} is the isotropic thermal expansion coefficient at T_0.

2.2 Water retention curve

To model thermal–hydro-mechanical properties of unsaturated soils, we need a general water retention model which is dependent on porosity and temperature of unsaturated soils. Here we adopt the water retention law proposed by [45], which reads

Table 1 Water retention material parameters [45]

Symbol	Value	Unit
a	0.038	kPa^{-1}
b	3.490	–
n	0.718	–
m	0.632	–
a_1	−608.0	K
b_1	1.0	–

$$S_r = \left\{ \frac{1}{1 + \left[a(v-1)^b \alpha_T s \right]^n} \right\}^m, \tag{9}$$

where v is the specific volume; α_T represents the temperature effect on the air-entry suction [45]; and

$$\alpha_T = \left(\frac{a_1 + b_1 T_0}{a_1 + b_1 T} \right)^{b_1}, \tag{10}$$

where n, m, a, b, a_1 and b_1 are material parameters. Table 1 shows the parameters of the water retention model for a sandy silt [45]. These material parameters are used to conduct the numerical simulations of thermal unsaturated soils presented in the section of numerical simulations.

Figure 1 shows water retention *curves* for three different specific volumes at three different temperatures.

2.3 Thermal plastic model

We use the (p', q, θ) representation to formulate the three stress-invariant constitutive model. The three stress-invariants are

$$p' = \frac{1}{3}\mathrm{tr}(\boldsymbol{\sigma}'), \quad q = \sqrt{\frac{3}{2}}||\boldsymbol{\xi}'||, \quad \frac{1}{\sqrt{6}}\cos(3\theta) = \frac{\mathrm{tr}\boldsymbol{\xi}'^3}{\chi^3}, \tag{11}$$

where q is the deviatoric stress, $\boldsymbol{\xi}' = \boldsymbol{\sigma}' - p'\boldsymbol{I}$, $\chi^2 = \mathrm{tr}(\boldsymbol{\xi}'^2)$ and θ is Lode's angle whose values range from $0 \leqslant \theta \leqslant \pi/3$.

It has been accepted that both suction and degree of saturation have a major impact on the yielding of the unsaturated soils under the isothermal conditions. Following [24], a bonding variable, which characterizes the overall effect of a meniscus between two soil particles and degree of saturation on the preconsolidation pressure, is written as follows [7],

$$\xi = f(s)(1 - S_r), \quad f(s) = 1 + \frac{s/p_{\mathrm{atm}}}{10.7 + 2.4(s/p_{\mathrm{atm}})}, \tag{12}$$

where $p_{\mathrm{atm}} = 101.3$ kPa is the atmospheric pressure, and $s = p_a - p_w$ is capillary pressure or suction.

Experimental study by Salager et al. [46] demonstrated that temperature increase tends to decrease the isotropic yield limit and a logarithmic function (i.e., the term $(1 - \gamma_T \log(T/T_0))$ in Eq. 13) fits well with the evolution of preconsolidation pressure with respect to temperature. To capture the experimentally observed physics, we proposed a preconsolidation pressure which is dependent on suction, degree of saturation [24] and temperature [32, 46] as follows,

$$\overline{p}_c = -\exp[a(\xi)](-p_c)^{b(\xi)}[1 - \gamma_T \log(T/T_0)], \tag{13}$$

where

$$a(\xi) = \frac{\tilde{N}[c(\xi) - 1]}{\tilde{\lambda}c(\xi) - \tilde{\kappa}}, \quad b(\xi) = \frac{\tilde{\lambda} - \tilde{\kappa}}{\tilde{\lambda}c(\xi) - \tilde{\kappa}}, \tag{14}$$
$$c(\xi) = 1 - c_1[1 - \exp(c_2\xi)],$$

$\tilde{\lambda}$ and $\tilde{\kappa}$ are compressibility parameters, and c_1 and c_2 are constants; $\tilde{N}$ is the specific volume when $p' = 1$ kPa; γ_T is a material parameter capturing the thermal evolution of preconsolidation pressure [21]; p_c is the preconsolidation pressure at the ambient temperature T_0 and zero suction. Like other constitutive models based on critical state theory, $\overline{p}_c$ serves as the hardening variable in this model.

Finally, the yield function is written as,

$$F = \zeta q + \eta p' \leqslant 0, \tag{15}$$

where

$$\eta = \begin{cases} M[1 + \ln(\overline{p}_i/p')] & \text{if} \quad N = 0, \\ (M/N)\left[1 - (1-N)(p'/\overline{p}_i)^{N/(1-N)}\right] & \text{if} \quad N > 0. \end{cases} \tag{16}$$

is the maximum stress ratio, and

$$\overline{p}_i = \begin{cases} \overline{p}_c/e & \text{if} \quad N = 0, \\ (1-N)^{(1-N)/N}\overline{p}_c & \text{if} \quad N > 0. \end{cases} \tag{17}$$

is an intermediate plastic internal variable [30]. Here M is the slope of the critical state line; N is the shape factor of the yield function; e is the natural number; $\zeta = \zeta(\rho, \theta)$ is a scaling function which reproduces the effect of ellipticity; and ρ is ellipticity of the yield surface on the deviatoric plane [8]. In this constitutive model, M is independent of temperature because the impact of temperature on M is arguable as elaborated by Masin and Khalili [35]. The associative flow rule is adopted in the constitutive model. As demonstrated by the numerical simulations in the section below, this thermal plastic constitutive model can capture the localized deformation even the normal flow rule is assumed. However, we can implement a similar plastic potential as the yield function in Eq. (15) if necessary. Figure 2 shows three yield surfaces in the principal

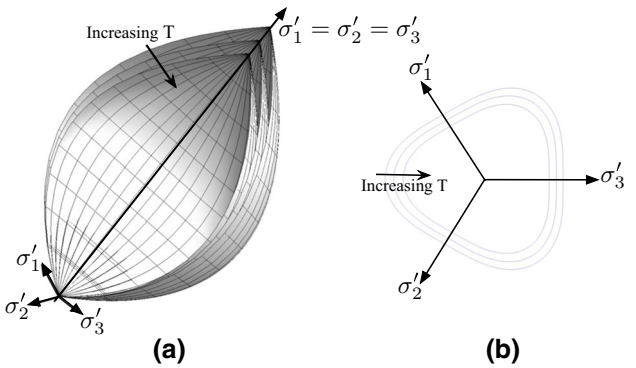

Fig. 2 **a** Yield surfaces in principal effective stress space; **b** cross sections on the deviatoric plane at three different temperatures

effective stress space and cross sections on the deviatoric plane at three different temperatures, respectively. Figure 2 implies that the increase in temperature decreases the size of yield surface of the solid skeleton. In other words, this thermal constitutive model can capture the soften effect of temperature on the solid skeleton.

3 Locally "drained" isothermal and adiabatic bifurcation analysis

The model described above is suitable for strain localization analysis into tabular deformation bands in thermal unsaturated soils. Here we formulate a criterion for the emergence of a tabular deformation band under the condition of locally "drained" deformation. This criterion can capture the impact of temperature through the thermal constitutive model for unsaturated soil. Furthermore, under the locally "drained" condition, the partially saturated soils can be treated as a single-phase material, i.e., the solid skeleton. Therefore, to derive the condition of the localized deformation, we can assume that the total traction on both sides of a shear band is continuous; the same constitutive model applies to the material within the localized band and the bulk; and the strain is discontinuous across the shear band at the inception of bifurcation.

3.1 Kinematics of a tabular band

To capture such a tabular deformation band, following the notation of [6, 7], a velocity field of the solid phase can be defined by the following ramp-like relation,

$$\boldsymbol{v} = \begin{cases} \bar{\boldsymbol{v}} & \text{if } \bar{\eta} \leqslant 0, \\ \bar{\boldsymbol{v}} + \bar{\eta}[\![\boldsymbol{v}]\!]/h & \text{if } 0 \leqslant \bar{\eta} \leqslant h, \\ \bar{\boldsymbol{v}} + [\![\boldsymbol{v}]\!] & \text{if } \bar{\eta} \geqslant h, \end{cases} \tag{18}$$

where $\bar{\boldsymbol{v}}$ is a continuous velocity field of the solid phase, $[\![\boldsymbol{v}]\!]$ represents the relative velocity of the opposite faces of the shear band, and h is the finite thickness of the shear band, and $\bar{\eta}$ is the distance of the solid material relative to the negative side the shear band. Assuming $[\![\boldsymbol{v}]\!]$ is uniform over the discontinuity $\mathcal{S}$, the corresponding velocity gradient fields outside and inside the band take the form

$$\boldsymbol{l} = \begin{cases} \nabla\bar{\boldsymbol{v}} & \text{in } \Omega\backslash\overline{\mathcal{D}}, \\ \nabla\bar{\boldsymbol{v}} + ([\![\boldsymbol{v}]\!] \otimes \boldsymbol{n})/h & \text{in } \mathcal{D}, \end{cases} \tag{19}$$

where Ω is the problem domain, $\mathcal{D}$ s the open shear band domain, $\overline{\mathcal{D}}$ is the closure of $\mathcal{D}$, and $\boldsymbol{n}$ is the unit normal vector to the band. By the relation $\dot{\boldsymbol{\epsilon}} = \mathrm{sym}(\boldsymbol{l})$ we readily obtain the strain rate within and outside the band

$$\dot{\boldsymbol{\epsilon}} = \begin{cases} \dot{\bar{\boldsymbol{\epsilon}}} & \text{in } \Omega\backslash\overline{\mathcal{D}}, \\ \dot{\bar{\boldsymbol{\epsilon}}} + \mathrm{sym}([\![\boldsymbol{v}]\!] \otimes \boldsymbol{n})/\mathrm{h} & \text{in } \mathcal{D}. \end{cases} \tag{20}$$

Assuming the same material law applies to the localized zone and the bulk, we can write out the jump of the total Cauchy stress rate across the shear band,

$$[\![\dot{\boldsymbol{\sigma}}]\!] = \boldsymbol{c} : [\![\dot{\boldsymbol{\epsilon}}]\!], \tag{21}$$

where $\boldsymbol{c}$ is the constitutive tangent operator with components $\boldsymbol{c} := \partial\boldsymbol{\sigma}/\partial\boldsymbol{\epsilon}$. Next, the continuity of the total traction across the shear band reads,

$$(\boldsymbol{c} : [\![\dot{\boldsymbol{\epsilon}}]\!]) \cdot \boldsymbol{n} = 0. \tag{22}$$

From Eq. (20), we get

$$[\![\dot{\boldsymbol{\epsilon}}]\!] = [\![\boldsymbol{v}]\!] \otimes \boldsymbol{n}/h. \tag{23}$$

Substituting Eq. (23) into Eq. (22) results in the jump condition,

$$\frac{1}{h}\boldsymbol{a} \cdot [\![\boldsymbol{v}]\!] = \boldsymbol{0},\ \boldsymbol{a} = \boldsymbol{n} \cdot \boldsymbol{c} \cdot \boldsymbol{n}, \tag{24}$$

where $\boldsymbol{a}$ is the so-called acoustic tensor [28]. For non-trivial solutions of the strain rate jump of the mixture, we obtain the localization condition,

$$\det \boldsymbol{a} = 0, \tag{25}$$

where det means the determinant of a tensor.

3.2 Locally "drained" isothermal bifurcation condition

For the locally "drained" condition, we assume both pore water and pore air pressures and temperature are continuous across the shear band. Therefore, the jumps of their rates equal to zero. Applying the jump operator on the rate form of Eq. (2), we have

$$[\![\dot{\boldsymbol{\sigma}}]\!] = \underbrace{\left[\frac{\partial\boldsymbol{\sigma}'}{\partial\boldsymbol{\epsilon}} + (p_a - p_w)\boldsymbol{I} \otimes \frac{\partial S_r}{\partial\boldsymbol{\epsilon}}\right]}_{\boldsymbol{c}^{\mathrm{ep}}} : [\![\dot{\boldsymbol{\epsilon}}]\!]. \tag{26}$$

Let $\boldsymbol{c}^{\mathrm{ep}} = \partial\boldsymbol{\sigma}'/\partial\boldsymbol{\epsilon}$ be the consistent thermal elasto-plastic tangent operator, where the superscript means the elasto-plastic. It is worth noting that $\overline{\boldsymbol{c}}^{\mathrm{ep}}$ equals to $\boldsymbol{c}^{\mathrm{ep}}$ if we assume S_r only depends on suction and temperature. In general, for thermal unsaturated soils, $\overline{\boldsymbol{c}}^{\mathrm{ep}}$ is dependent on the strain of the solid phase, suction, degree of saturation and temperature of the mixture. From Eq. (24), the drained acoustic tensor takes the form

$$\boldsymbol{a} = \boldsymbol{n} \cdot \overline{\boldsymbol{c}}^{\mathrm{ep}} \cdot \boldsymbol{n}. \tag{27}$$

To determined $\overline{\boldsymbol{c}}^{\mathrm{ep}}$ we need to compute $\boldsymbol{c}^{\mathrm{ep}}$ and $\dfrac{\partial S_r}{\partial \boldsymbol{\epsilon}}$. The latter can be readily determined by Eq. (9) since the specific volume v is a function of volumetric strains of soils. However, it is non-trivial to determine $\boldsymbol{c}^{\mathrm{ep}}$. Next, we derive a spectral representation of $\boldsymbol{c}^{\mathrm{ep}}$ from a local numerical implementation of the constitutive model via the return mapping algorithm for computational plasticity [51].

3.3 Spectral representation of the consistent tangent operator

This proposed model was implemented numerically at the material point level via the return mapping algorithm. As a by-product of the numerical implementation, the temperature-dependent consistent tangent operator is readily accessible for the bifurcation analysis. For this three-invariant model, the return mapping algorithm is implemented in principal elastic strain space via the spectral decomposition of the strain tensor. The motivation of using the spectral representation is twofold. Firstly, the numerical implementation in the principal strain space will reduce the residual equations from seven to four (see Eq. 34) for the infinitesimal deformation case considered in this paper, which will reduce the computational cost for a large-scale simulation (e.g., a field-scale problem). Secondly, as a by-product of the material integration subroutine, we can readily express the thermal–hydro-mechanical consistent tangent operator $\boldsymbol{c}^{\mathrm{ep}}$ in the spectral form at a time step $n+1$. First, we can derive $\boldsymbol{c}^{\mathrm{ep}}$ through the chain rule,

$$\boldsymbol{c}^{\mathrm{ep}} = \frac{\partial\boldsymbol{\sigma}'}{\partial\boldsymbol{\epsilon}} \equiv \frac{\partial\boldsymbol{\sigma}'}{\partial\boldsymbol{\epsilon}^{e,\mathrm{tr}}} = \frac{\partial\boldsymbol{\sigma}'}{\partial\boldsymbol{\epsilon}^{\mathrm{e}}} : \frac{\partial\boldsymbol{\epsilon}^{\mathrm{e}}}{\partial\boldsymbol{\epsilon}^{e,\mathrm{tr}}}, \tag{28}$$

where $\boldsymbol{\epsilon}$, $\boldsymbol{\epsilon}^{\mathrm{etr}}$ and $\boldsymbol{\epsilon}^{\mathrm{e}}$ are the total strain, the trial elastic strain, and the real elastic strain at the time step $n+1$, respectively; and tr means trial.

The effective Cauchy stress tensor and the elastic strain tensor in their spectral forms are written as,

$$\boldsymbol{\sigma}' = \sum_{A=1}^{3} \sigma'_A \boldsymbol{m}^{(A)}, \quad \boldsymbol{\epsilon}^{e} = \sum_{A=1}^{3} \epsilon^{e}_A \boldsymbol{m}^{(A)}, \quad \boldsymbol{\epsilon}^{e,\mathrm{tr}} = \sum_{A=1}^{3} \epsilon^{e,\mathrm{tr}}_A \boldsymbol{m}^{(A)}, \tag{29}$$

where $\boldsymbol{m}^{(A)} = \boldsymbol{n}^{(A)} \otimes \boldsymbol{n}^{(A)}$ is the spectral direction constructed from unit vector $\boldsymbol{n}^{(A)}$ in the direction of principal stress σ'_A.

The spectral form of the elastic tangent modulus $\boldsymbol{c}^{\mathrm{e}} = \partial\boldsymbol{\sigma}'/\partial\boldsymbol{\epsilon}^{\mathrm{e}}$ (a fourth-order tensor) can be expressed as

$$\boldsymbol{c}^{\mathrm{e}} = \sum_{A=1}^{3}\sum_{B=1}^{3} \mathcal{A}^{\mathrm{e}}_{AB} \boldsymbol{m}^{(\mathrm{A})} \otimes \boldsymbol{m}^{(\mathrm{B})} + \frac{1}{2}\sum_{A=1}^{3}\sum_{B\neq A} \left(\frac{\sigma'_B - \sigma'_A}{\epsilon^{\mathrm{e}}_B - \epsilon^{\mathrm{e}}_A}\right) \left(\boldsymbol{m}^{(AB)} \otimes \boldsymbol{m}^{(AB)} + \boldsymbol{m}^{(AB)} \otimes \boldsymbol{m}^{(BA)}\right), \tag{30}$$

where $\boldsymbol{m}^{(AB)} = \boldsymbol{n}^{(A)} \otimes \boldsymbol{n}^{(B)}$ and $\mathcal{A}^{\mathrm{e}}_{AB}$ is the element with index AB of the tangential elasticity matrix in principal axes. Similarly the spectral form of $\boldsymbol{\alpha} = \partial\boldsymbol{\epsilon}^{\mathrm{e}}/\partial\boldsymbol{\epsilon}^{e,\mathrm{tr}}$ (a fourth-order tensor) is

$$\boldsymbol{\alpha} = \sum_{A=1}^{3}\sum_{B=1}^{3} \frac{\partial\epsilon^{\mathrm{e}}_A}{\partial\epsilon^{e,\mathrm{tr}}_B} \boldsymbol{m}^{(\mathrm{A})} \otimes \boldsymbol{m}^{(\mathrm{B})} + \frac{1}{2}\sum_{A=1}^{3}\sum_{B\neq A} \left(\frac{\epsilon^{\mathrm{e}}_B - \epsilon^{\mathrm{e}}_A}{\epsilon^{e,\mathrm{tr}}_B - \epsilon^{e,\mathrm{tr}}_A}\right) \left(\boldsymbol{m}^{(AB)} \otimes \boldsymbol{m}^{(AB)} + \boldsymbol{m}^{(AB)} \otimes \boldsymbol{m}^{(BA)}\right). \tag{31}$$

Substituting Eqs. (30) and (31) into Eq. (28), we obtain the consistent tangent operator in the spectral form,

$$\boldsymbol{c}^{\mathrm{ep}} = \sum_{A=1}^{3}\sum_{B=1}^{3} \mathcal{A}_{AB} \boldsymbol{m}^{(A)} \otimes \boldsymbol{m}^{(B)} + \frac{1}{2}\sum_{A=1}^{3}\sum_{B\neq A} \left(\frac{\sigma'_B - \sigma'_A}{\epsilon^{e,\mathrm{tr}}_B - \epsilon^{e,\mathrm{tr}}_A}\right) \left(\boldsymbol{m}^{(AB)} \otimes \boldsymbol{m}^{(AB)} + \boldsymbol{m}^{(AB)} \otimes \boldsymbol{m}^{(BA)}\right), \tag{32}$$

where

$$\mathcal{A}_{AB} = \frac{\partial\sigma'_A}{\partial\epsilon^{e,\mathrm{tr}}_B} = \sum_{K=1}^{3} \frac{\partial\sigma'_A}{\partial\epsilon^{e}_K} \frac{\partial\epsilon^{e}_K}{\partial\epsilon^{e,\mathrm{tr}}_B} = \sum_{K=1}^{3} \mathcal{A}^{e}_{AK} \frac{\partial\epsilon^{e}_K}{\partial\epsilon^{e,\mathrm{tr}}_B}, \tag{33}$$

which needs to be calculated from the material point integration subroutine as briefly described next.

From load step n to load step $n+1$, suppose we know $\boldsymbol{\epsilon}_n$, s_n and T_n at time n, and given $\Delta\boldsymbol{\epsilon}$, Δs and ΔT, we need to calculate the stress $\boldsymbol{\sigma}'$ and internal variables (i.e., $\overline{p_i}$) at load step $n+1$. We define

$$\boldsymbol{r} = \boldsymbol{r}(\boldsymbol{x}, \boldsymbol{z}) = \left\{ \begin{array}{c} \epsilon^{e}_1 - \epsilon^{e,\mathrm{tr}}_1 + \Delta\lambda\partial_{\sigma'_1} F \\ \epsilon^{e}_2 - \epsilon^{e,\mathrm{tr}}_2 + \Delta\lambda\partial_{\sigma'_2} F \\ \epsilon^{e}_3 - \epsilon^{e,\mathrm{tr}}_3 + \Delta\lambda\partial_{\sigma'_3} F \\ F(\sigma'_1, \sigma'_2, \sigma'_3, \bar{p}_c) \end{array} \right\}\Bigg|_{n+1}, \tag{34}$$

with

$$\boldsymbol{x} = \left\{ \begin{array}{c} \epsilon^{e}_1 \\ \epsilon^{e}_2 \\ \epsilon^{e}_3 \\ \Delta\lambda \end{array} \right\}\Bigg|_{n+1}, \quad \boldsymbol{z} = \left\{ \begin{array}{c} \epsilon^{e,\mathrm{tr}}_1 \\ \epsilon^{e,\mathrm{tr}}_2 \\ \epsilon^{e,\mathrm{tr}}_3 \\ s^{\mathrm{tr}} \\ T^{\mathrm{tr}} \end{array} \right\}\Bigg|_{n+1}, \tag{35}$$

where $\boldsymbol{r}$ is a residual vector, and $\Delta\lambda \geqslant 0$ is the standard incremental plastic multiplier. Here $\boldsymbol{x}$ contains the local independent variables that satisfy the constitutive laws for a given $\boldsymbol{z}$, whereas $\boldsymbol{z}$ contains the increment of strains, suction and temperature at the load step, $n+1$. From this point of view, we can assume $\boldsymbol{x}$ is dependent on $\boldsymbol{z}$. The solution of the problem at a local stress point is the vector $\bar{\boldsymbol{x}}$ such that $\boldsymbol{r}(\bar{\boldsymbol{x}}) = 0$ for a given $\boldsymbol{z}$. To solve the nonlinear equations, we use Newton's method to compute $\boldsymbol{x}$ at time step $n+1$.

To obtain the elements for the consistent tangent operator, we can differentiate $\boldsymbol{r}$ with respect to $\boldsymbol{z}$ at $\boldsymbol{x} = \bar{\boldsymbol{x}}$ to get

$$\frac{\partial \boldsymbol{r}}{\partial \boldsymbol{z}} = \left.\frac{\partial \boldsymbol{r}}{\partial \boldsymbol{z}}\right|_{\boldsymbol{x}} + \underbrace{\left(\left.\frac{\partial \boldsymbol{r}}{\partial \boldsymbol{x}}\right|_{\boldsymbol{z}}\right)}_{\boldsymbol{A}} \cdot \frac{\partial \boldsymbol{x}}{\partial \boldsymbol{z}} = \boldsymbol{0}, \tag{36}$$

where $\boldsymbol{A}$ is a 4×4 matrix. Given that the local iteration at a material point has converged, we can solve Eq. (36) and have

$$\frac{\partial \boldsymbol{x}}{\partial \boldsymbol{z}} = -\boldsymbol{B} \cdot \left.\frac{\partial \boldsymbol{r}}{\partial \boldsymbol{z}}\right|_{\boldsymbol{x}}, \tag{37}$$

where $\boldsymbol{B} = \boldsymbol{A}^{-1}$. Expanding Eq. (37) yields

$$\begin{bmatrix} \partial \overline{\boldsymbol{\epsilon}}^{\mathrm{e}} / \partial \overline{\boldsymbol{\epsilon}}^{e,\mathrm{tr}} & \partial \overline{\boldsymbol{\epsilon}}^{\mathrm{e}} / \partial s^{\mathrm{tr}} & \partial \overline{\boldsymbol{\epsilon}}^{\mathrm{e}} / \partial T^{\mathrm{tr}} \\ \partial \Delta\lambda / \partial \overline{\boldsymbol{\epsilon}}^{e,\mathrm{tr}} & \partial \Delta\lambda / \partial s^{\mathrm{tr}} & \partial \Delta\lambda / \partial T^{\mathrm{tr}} \end{bmatrix} = -\begin{bmatrix} \boldsymbol{B}_{11} & \boldsymbol{B}_{12} \\ \boldsymbol{B}_{21} & B_{22} \end{bmatrix} \begin{bmatrix} \boldsymbol{C}_{11} & \boldsymbol{C}_{12} & \boldsymbol{C}_{13} \\ \boldsymbol{C}_{21} & C_{22} & C_{23} \end{bmatrix}, \tag{38}$$

where $\overline{\boldsymbol{\epsilon}}^{\mathrm{e}}$ and $\overline{\boldsymbol{\epsilon}}^{e,\mathrm{tr}}$ are vectors whose elements are three principal elastic strains and three principal trial elastic strains, respectively. $\boldsymbol{B}_{11}$ is a 3×3 matrix; $\boldsymbol{B}_{12}$ and $\boldsymbol{B}_{21}$ are a 1×3 vector and a 3×1 vector, respectively; and B_{22} is a scalar; and the submatrices for $\boldsymbol{C}$ are

$$\boldsymbol{C}_{11} = \Delta\lambda \partial^2_{\overline{\boldsymbol{\sigma}}' \bar{p}_c} F \otimes \partial_{\boldsymbol{\epsilon}^{e,\mathrm{tr}}} \bar{p}_c - \boldsymbol{I}, \tag{39}$$

$$\boldsymbol{C}_{12} = \Delta\lambda \partial^2_{\overline{\boldsymbol{\sigma}}' \bar{p}_c} F \times \partial_{s^{\mathrm{tr}}} \bar{p}_c, \tag{40}$$

$$\boldsymbol{C}_{13} = \Delta\lambda \partial^2_{\overline{\boldsymbol{\sigma}}' \bar{p}_c} F \times \partial_{T^{\mathrm{tr}}} \bar{p}_c, \tag{41}$$

$$\boldsymbol{C}_{21} = \partial_{\bar{p}_c} F \times \partial_{\boldsymbol{\epsilon}^{e,\mathrm{tr}}} \bar{p}_c, \tag{42}$$

$$C_{22} = \partial_{\bar{p}_c} F \times \partial_{s^{\mathrm{tr}}} \bar{p}_c, \tag{43}$$

$$C_{23} = \partial_{\bar{p}_c} F \times \partial_{T^{\mathrm{tr}}} \bar{p}_c, \tag{44}$$

where $\overline{\boldsymbol{\sigma}}'$ is a vector whose elements are three principal effective stresses. We thus obtain

$$\partial \overline{\boldsymbol{\epsilon}}^{\mathrm{e}} / \partial \overline{\boldsymbol{\epsilon}}^{e,\mathrm{tr}} = -\boldsymbol{B}_{11} \cdot \boldsymbol{C}_{11} - \boldsymbol{B}_{12} \otimes \boldsymbol{C}_{21}, \tag{45}$$

$$\partial \overline{\boldsymbol{\epsilon}}^{\mathrm{e}} / \partial T^{\mathrm{tr}} = -\boldsymbol{B}_{11} \cdot \boldsymbol{C}_{13} - \boldsymbol{B}_{12} \times C_{23}. \tag{46}$$

Note that $\partial \overline{\boldsymbol{\epsilon}}^{\mathrm{e}} / \partial \overline{\boldsymbol{\epsilon}}^{e,\mathrm{tr}}$ is a second-order tensor with components $[\partial \overline{\boldsymbol{\epsilon}}^{\mathrm{e}} / \partial \overline{\boldsymbol{\epsilon}}^{e,\mathrm{tr}}]_{ij} = \partial \epsilon_i^{\mathrm{e}} / \partial \epsilon_j^{e,\mathrm{tr}}$ $(i,j = 1,2,3)$. Finally, substituting $\partial \epsilon_i^{\mathrm{e}} / \partial \epsilon_j^{e,\mathrm{tr}}$ $(i,j = 1,2,3)$ into Eqs. (33) and (32), we can compute the consistent thermal elasto-plastic tangent operator $\boldsymbol{c}^{ep}$ from the material integration subroutine.

3.4 Locally "drained" adiabatic bifurcation condition

For the adiabatic process, we assume the heat flux and heat source are zero [19, 50]. To derive a thermal elasto-plastic tangent operator under the locally drained and adiabatic conditions, we need two coupled evolution equations for the effective stress and temperature, respectively [19]. Following the derivation by Semnani et al. [50] for a thermal single-phase material under the adiabatic condition, we may write out the heat conduction equation of a material point in unsaturated soils under the locally drained and adiabatic conditions as,

$$\rho c \dot{T} = \zeta_T \boldsymbol{\sigma}' : \dot{\boldsymbol{\epsilon}}^p, \tag{47}$$

where c is the heat capacity per unit mass; T denotes the absolute temperature; and ζ_T describes the portion of plastic work converted into heat. In this paper, we assume $\zeta_T = 1.0$ [50]. Using the additive split of total strain rate, we can write

$$\dot{T} = \frac{\zeta_T}{\rho c} \boldsymbol{\sigma}' : \left(\dot{\boldsymbol{\epsilon}} - \dot{\boldsymbol{\epsilon}}^e - \dot{\boldsymbol{\epsilon}}^e_T\right) = \frac{\zeta_T}{\rho c} \boldsymbol{\sigma}' : \left(\dot{\boldsymbol{\epsilon}} - \dot{\boldsymbol{\epsilon}}^e - \frac{1}{3} \boldsymbol{I} \beta_s \dot{T}\right) \tag{48}$$

Solving $\dot{T}$ yields

$$\dot{T} = \frac{\zeta_T}{\phi_T} (\boldsymbol{\sigma}' : \dot{\boldsymbol{\epsilon}} - \boldsymbol{\sigma}' : \dot{\boldsymbol{\epsilon}}^e), \tag{49}$$

where $\phi_T = 1 - \beta_s \zeta_T / (3\rho c) \boldsymbol{\sigma}' : \boldsymbol{I} = 1 - \beta_s \zeta_T p' / (\rho c)$. Referring to Eq. (28), we can write the rate form of the effective stress under the locally drained and adiabatic conditions as,

$$\dot{\boldsymbol{\sigma}}' = \boldsymbol{c}^{ep} : \dot{\boldsymbol{\epsilon}} + \boldsymbol{\tau} \dot{T}, \tag{50}$$

where $\boldsymbol{\tau} = \partial \boldsymbol{\sigma}' / \partial T = (\partial \boldsymbol{\sigma}' / \partial \boldsymbol{\epsilon}^e) : (\partial \boldsymbol{\epsilon}^e / \partial T)$. Similarly to the derivation of $\boldsymbol{c}^{ep}$, the spectral form of $\boldsymbol{\tau}$ can be written as

$$\boldsymbol{\tau} = \sum_{A=1}^{3} \sum_{K=1}^{3} \frac{\partial \sigma'_A}{\partial \epsilon^e_K} \frac{\partial \epsilon^e_K}{\partial T} \boldsymbol{m}^{(A)} = \sum_{A=1}^{3} \sum_{K=1}^{3} \mathcal{A}^e_{AK} \frac{\partial \epsilon^e_K}{\partial T} \boldsymbol{m}^{(A)} \tag{51}$$

where $\partial \epsilon^e_K / \partial T$ is determined by Eq. (46). Here we assume the rotation of principle axes is determined by $\boldsymbol{\epsilon}^{e,\mathrm{tr}}$ alone (refer to Borja et al. [9] for more elaboration).

Substituting Eq. (49) into (50) and rearranging terms yield

$$\mathscr{L}^{-1} : \dot{\boldsymbol{\sigma}}' = \mathscr{B} : \dot{\boldsymbol{\epsilon}}, \tag{52}$$

where

$$\mathscr{L}^{-1} = \mathbb{I} + \frac{\zeta_T}{\phi_T \rho c}\boldsymbol{\tau} \otimes (\boldsymbol{\sigma}' : (\boldsymbol{c}^e)^{-1}), \tag{53}$$

$$\mathscr{B} = \boldsymbol{c}^{ep} + \frac{\zeta_T}{\phi_T \rho c}\boldsymbol{\tau} \otimes \boldsymbol{\sigma}'. \tag{54}$$

In Eq. (53), $\mathbb{I}$ is the fourth-order symmetric identity tensor with components $(\mathbb{I})_{ijkl} = (\delta_{ik}\delta_{jl} + \delta_{il}\delta_{jk})/2$. We thus obtain the tangent thermoelastoplastic constitutive relationship under the adiabatic condition as,

$$\dot{\boldsymbol{\sigma}}' = \boldsymbol{c}^{ept} : \dot{\boldsymbol{\epsilon}}, \quad \boldsymbol{c}^{ept} = \mathscr{L} : \mathscr{B}. \tag{55}$$

Here we shall call $\boldsymbol{c}^{ept}$ as the consistent thermoelastoplastic tangential moduli tensor, which is analogous to the undrained tangential moduli tensor in unsaturated soil problems under the isothermal conditions [7]. Similarly to Eq. (26), we can express the effective consistent thermoelastoplastic tangential moduli tensor taking into account the volumetric strain dependence of degree of saturation as,

$$\overline{\boldsymbol{c}}^{ept} = \boldsymbol{c}^{ept} + (p_a - p_w)\boldsymbol{1} \otimes \frac{\partial s_r}{\partial \boldsymbol{\epsilon}}. \tag{56}$$

Then the thermoelastoplastic acoustic tensor under locally drained and adiabatic conditions can be written as,

$$\boldsymbol{a}^{ept} = \boldsymbol{n} \cdot \overline{\boldsymbol{c}}^{ept} \cdot \boldsymbol{n}. \tag{57}$$

The term $\boldsymbol{a}^{ept}$ is analogous to the undrained acoustic tensor used in the bifurcation analysis of unsaturated soils [7].

4 Isothermal and adiabatic bifurcation analysis under plane strain condition

Localized failure analysis of three-phase porous media under the non-isothermal conditions as a boundary value problem relies on the bifurcation analysis at the material point level. In the section, we conduct the locally "drained" isothermal and adiabatic bifurcation analysis at the constitutive level. Specifically we conduct the drained bifurcation analysis of thermal unsaturated soils under the plane strain condition via the derived drained bifurcation condition under non-thermal conditions. Note that the drained acoustic tensor is dependent on both temperature and suction through the thermal plastic constitutive model. The material parameters for the thermal plastic constitutive model are shown in Table 2.

For all simulations presented in this section, the reference temperature (the ambient temperature) is assumed to be 22 °C, and the time increment $\Delta t = 1$ s of each load step. We assume the initial effective stress on the solid phase are $\sigma'_{11} = \sigma'_{22} = \sigma'_{33} = -100$ kPa which represent an isotropic stress condition. The initial specific volume of all samples with the exception of the sample for an initial density sensitivity analysis is assumed equal to 1.58. All simulations are conducted under the plane strain condition. We first simulate the locally drained and isothermal bifurcation under the plane strain condition at four different temperatures. Secondly, we present numerical simulations of the locally drained and isothermal bifurcation under the plane strain condition by imposing both mechanical and thermal loads. We then analyze the sensitivity of the numerical results to the initial density. Finally, we study the locally drained and adiabatic bifurcation under the plane strain condition at four different temperatures.

Table 2 Material parameters for the thermal plastic constitutive model (note: for the hyper-elastic model both α and ϵ^e_{v0} are assumed to be zero

Symbol	Value	Parameter
$\tilde{\kappa}$	0.03	Elastic compressibility index
p_0	−0.1 MPa	Reference mean stress
μ_0	10 MPa	Shear modulus
β_{s0}	6.67×10^{-4}	The constant thermal expansion coefficient [21]
M_0	1.1	Critical state parameter at ambient temperature
$\tilde{\lambda}$	0.11	Plastic compressibility index
v_{c0}	1.85	Reference specific volume
N	0.4	Shape factor of yield function
ρ	0.779	Ellipticity
c_1	0.185	Parameter of ξ [24]
c_2	1.49	Parameter of ξ [24]
γ_T	0.23	Thermal parameter for the preconsolidation pressure [21]

For the plastic model, the parameters are referred to [30])

4.1 Locally drained isothermal bifurcation at constant elevated temperature

For this example, we impose the strain increments per load step (second), $\Delta\epsilon_{11} = 0.0005$, $\Delta\epsilon_{22} = -0.001$, and all other $\Delta\epsilon_{ij} = 0$ (plane strain on the 12-plane). In the first case, we assume a constant suction of 10 kPa. We run simulations at four constant temperatures, 22, 40, 60 and 80 °C, to study the impact of the elevated temperature on the locally drained and isothermal bifurcation of unsaturated soils. Figure 3 shows the variation of determinant function with the band orientation when the determinant of the locally drained and isothermal acoustic tensor becomes negative for the first time at these four temperatures, respectively. Figure 3 illustrates that the localized deformation occurs at the load step of 7 (or equivalent 7 s) at the elevated temperature of 80 °C while for other simulations at lower

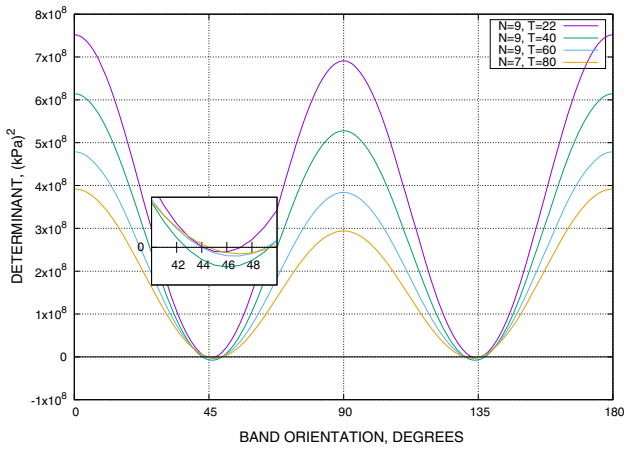

Fig. 3 Variation of determinant function with the band orientation at four different temperatures and $s = 10$ kPa. *Note N* is the load step number, and T is temperature (unit: °C)

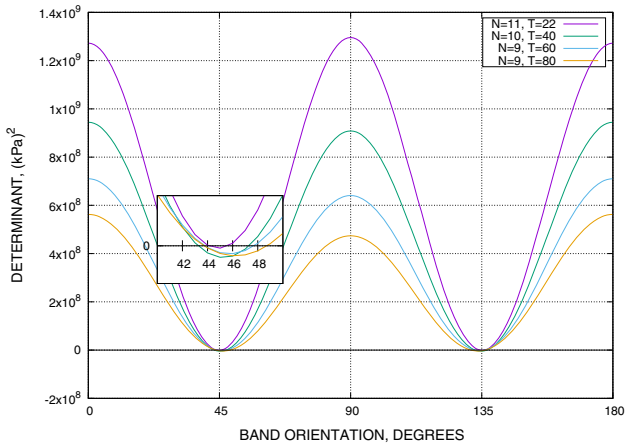

Fig. 4 Variation of determinant function with the band orientation at four different temperatures and $s = 20$ kPa. *Note N* is the load step number, and T is temperature (unit: °C)

temperatures the localized deformation occurs at a load time step of 9 (or equivalent 9 s). The critical band orientations in Fig. 3 show two conjugate shear bands may form in the sample. For this reason, only zoom-in portion of the critical directions of shear band near 45° is presented for all simulations. The zoom-in portion in Fig. 3 indicates that both the critical direction for localized failure and its range vary with temperature.

For the second case, we assume a constant suction of 20 kPa. Figure 4 shows the variations of determinant function with the band orientation when the determinant of the locally drained and isothermal acoustic tensor becomes negative for the first time at the four temperatures. For this case, the localized failures occur at larger strains for all elevated temperatures, compared to the results at $s = 10$ kPa presented in Fig. 3. This may be interpreted by the fact that a higher suction expands the initial yield surface at all elevated temperatures. Therefore, it requires a larger strain to initiate localized failures. Figure 4 indicates that the number of load steps (or equivalently total strains imposed on the sample) to trigger a localized failure decreases when the sample temperature increases. The zoom-in portion in Fig. 4 illustrates the range of critical direction of shear band increases when temperature increases. This may imply a thermal softening phenomenon in unsaturated soils.

4.2 Locally drained isothermal bifurcation under mechanical and thermal loads

Assuming the same initial effective stress state as used for the simulations above, we conduct the plane strain compression by imposing both mechanical and thermal loads. The temperature increment per load step (second) is 1 °C. To study the temperature effect on the potential localized deformation, the strain increments for each load step $\Delta t = 1$ s are assumed $\Delta\epsilon_{11} = 0.00005$ and $\Delta\epsilon_{22} = -0.0001$ on the 12-plane for the material point. We first conduct the simulation at a lower suction, $s = 10$ kPa.

Figure 5 shows the results of localization analysis of samples under both mechanical and thermal loading at a constant suction of 10 kPa. The results at the constant ambient temperature is also shown in Fig. 5. Figure 5 demonstrates that the localized failure occurs for the first time at the load step of 19 (or equivalent 19 s) when sample temperature increases to 51 °C. However, for the simulation at constant ambient temperature, the localized failure occurs for the first time at a load step of 24 (or equivalently 24 s). Furthermore, the zoom-in plot of Fig. 5 shows that the range of critical direction of shear band increases under both mechanical and thermal loads. The simulation results demonstrate that the elevated temperature may cause unsaturated soils to be more susceptible to localized failure.

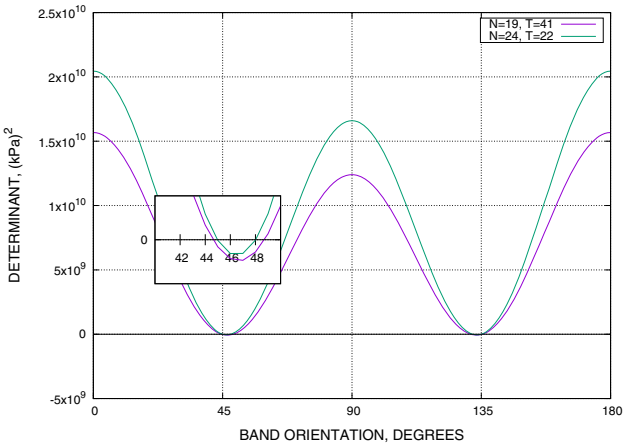

Fig. 5 Variation of determinant function with the band orientation under both the mechanical and thermal loads at $s = 10$ kPa. *Note N* is the load step number, and T is temperature (unit: °C)

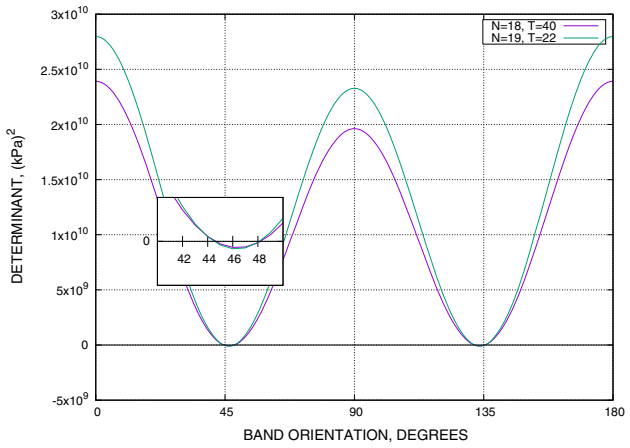

Fig. 6 Variation of determinant function with the band orientation under both the mechanical and thermal loads at $s = 20$ kPa. *Note N* is the load step number, and T is temperature (unit: °C)

Table 3 Summary of the timing, total strains and temperature upon bifurcation of samples under both mechanical and thermal loads

Suction (kPa)	Total loading time (s)	Total strains	Final temperature (°)
10	19	$\epsilon_{11} = 0.0095$, $\epsilon_{22} = -0.019$	51
10	24	$\epsilon_{11} = 0.0120$, $\epsilon_{22} = -0.024$	22 (fixed ambient temperature)
20	18	$\epsilon_{11} = 0.0090$, $\epsilon_{22} = -0.018$	40
20	19	$\epsilon_{11} = 0.0095$, $\epsilon_{22} = -0.019$	22 (fixed ambient temperature)

We also conduct similar simulations at $s = 20$ kPa. For this case, we assume the same mechanical and thermal loading rates for the simulation at $s = 10$ kPa. Figure 6 presents the localized failure analysis for this case as well as the simulations at the constant ambient temperature. Figure 6 illustrates that the determinant function becomes negative for the first time at a load step of 18 (or equivalently 18 s) with a temperature of 40 °C while the determinant function becomes negative for the first time at a load step of 19 (or equivalent 19 s) at the constant ambient temperature. The zoom-in part of Fig. 6 highlights that the range of the negative determinant at the onset of a localized failure for both simulations with and without a thermal loading are similar. Comparing Figs. 4 and 5, Table 3, we may conclude that the thermal effect on the inception of bifurcation may be reduced by the increased suction state in the soil sample. In other words, compared to the suction the temperature may be a secondary factor affecting the initiation of a localized deformation in unsaturated soils under the same mechanical loading condition.

4.3 Sensitivity of locally drained isothermal bifurcation to initial density

The initial dry density may impact the inception of localized deformation in unsaturated soils. To study the sensitivity of the localized deformation to the initial dry density, we run simulations with three different initial dry density of unsaturated soils. For all simulations, the assumed suction is 10 kPa. The three initial specific volumes are 1.55, 1.58 and 1.61, respectively. The initial temperature is 22 °C. According to Eq. (9), the initial degree of saturation are 0.937, 0.927 and 0.918, respectively. The strain and temperature increments per load step, $\Delta t = 1s$ are $\Delta\epsilon_{11} = 0.0005$, $\Delta\epsilon_{22} = -0.001$, and $\Delta T = 1\,^{\circ}\mathrm{C}$, respectively.

Figure 7 presents the variation of the determinant function with the band orientation when the determinant first becomes negative for these three cases. Figure 7 implies that the determinant functions are similar to each other upon the inception of localized deformation though the ranges of the band orientation are different as shown in the zoom-in portion. However, the smaller initial specific volume requires larger strains and higher temperature (or equivalently longer loading time) to trigger a localized deformation. For example, upon the inception of localized deformation, for the sample with an initial specific volume of 1.55 the imposed strains are $\epsilon_{11} = 0.0135$ and $\epsilon_{22} = -0.027$, and the final temperature is 49 °C. While for the sample with an initial specific volume of 1.61 the imposed strains are $\epsilon_{11} = 0.011$ and $\epsilon_{22} = -0.022$, and the final temperature is 44 °C.

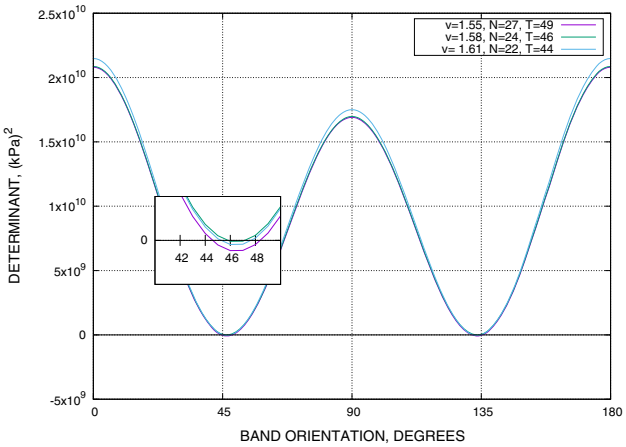

Fig. 7 Variation of determinant function with the band orientation for three different initial specific volumes at $s = 10$ kPa. *Note N* is the load step number, and T is temperature (unit: °C)

4.4 Locally drained adiabatic bifurcation at constant elevated temperature

In this part, we study the thermal impact on the inception of localized failures of unsaturated soils under the locally drained and adiabatic conditions. Here by assuming a locally drained condition we aim to highlight the thermal effect generated by the plastic deformation on localized failures in unsaturated soils. In addition to the material parameters for the isothermal bifurcation analysis, we assume a normalized heat capacity parameter $\bar{c} = c/c_0 \times 10^3$ with $c_0 = 703\,\mathrm{J/(kg\,K)}$ [50]. Furthermore, the density of the soil skeleton is assumed as $\rho = 2000\,\mathrm{kg/m^3}$. The same loading rates used for the examples in Sect. 4.1 are adopted. To study the locally drained adiabatic bifurcation, we run simulations at four different temperatures with a constant suction of 20 kPa. Figure 8 portrays the variations of determinant function with the band orientation when the determinant of the adiabatic acoustic tensor under the locally drained condition becomes negative for the first time at the four temperatures. Figure 8 demonstrates that localized failure occurs at a lower load step number (equivalent smaller strains) as detected by the adiabatic bifurcation condition (Eq. 57) than that predicted by the isothermal bifurcation condition as shown in Fig. 4. This may be interpreted by the thermal softening generated by the plastic work under the adiabatic condition. Therefore, bifurcation is detected at lower values of strain. As discussed by Semnani et al. [50], here we assume a smaller value of c to illustrate the thermal effects that may occur because of larger plastic deformations.

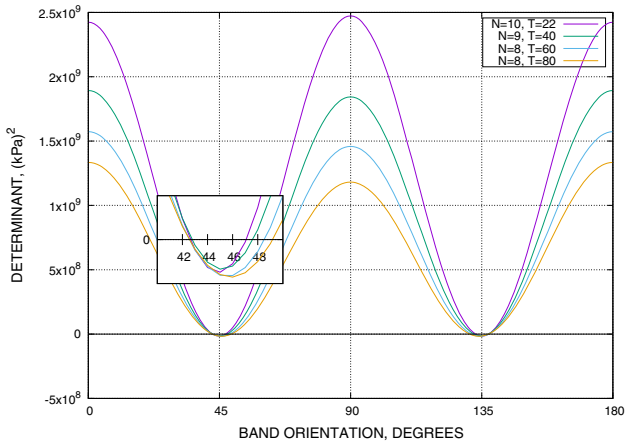

Fig. 8 Variation of determinant function with the band orientation at four different temperatures and $s = 20$ kPa. *Note N* is the load step number, and T is temperature (unit: °C)

5 Summary and conclusions

We presented a locally drained isothermal and adiabatic bifurcation analysis of thermal unsaturated soils via a recently proposed meso-scale thermal plastic model for unsaturated soils. We derived the kinematics of a tabular band formed in unsaturated soils under the locally drained condition via the infinitesimal strain theory. We also formulated a spectral representation of the locally drained consistent tangent operator which is dependent on both temperature and suction via the thermal plastic constitutive model. This spectral representation was utilized to detect the negative value of the determinant at the onset of localized failure and to compute the critical angle of the localized failure. Assuming a constant suction, the numerical simulations of unsaturated soils at the constitutive level were conducted under plane strain condition at elevated constant temperatures. We also ran similar simulations under both mechanical and thermal loading until localized failure occurs. The results were compared with the results obtained at constant ambient temperature. A negative determinant function and the critical angle of localized failure were shown to be dependent on the temperature. Under similar hydro-mechanical and boundary conditions, the elevated temperature may cause an unsaturated soil to be more susceptible to localized failure. Furthermore, the simulations showed that the initial density may affect the timing and orientation of bifurcation in thermal unsaturated soils. The numerical modeling also demonstrated that adiabatic bifurcation condition may predict an earlier bifurcation than isothermal bifurcation under a locally drained condition. The findings and the spectral representation of the consistent thermal plastic tangent operator in this article are useful for conducting localized failure analysis in thermal unsaturated soils at the specimen level as a boundary value problem, for example, persistent shear banding triggered by thermal fluctuations in such materials.

The aforementioned simulations were conducted at the material point level assuming infinitesimal deformation under suction-controlled plane strain condition. The objective here was to probe how the temperature could affect the timing and the critical angle of bifurcation of unsaturated soils. Preliminary results show that the elevated temperature and the initial density affect the timing and critical orientations of bifurcation, though this influence is not as dramatic as the one caused by mechanical loading. The simulations do not include the local fluid flow and its impact on the inception of bifurcation in unsaturated soils. Further study will be needed to incorporate this local condition when modeling unsaturated soils under the non-isothermal conditions. To the authors' knowledge, there are

no such laboratory results available in the literature. Therefore, experiments will be conducted in the future to validate the numerical results. Furthermore, the simulations of soil samples as an initial boundary value problem at the specimen level are required to investigate the thermal bifurcation of unsaturated soils as a multiphysical process.

Acknowledgements The authors are grateful to the anonymous reviewers for their constructive reviews. Their comments were truly helpful in improving the paper from its first version.

References

1. Alonso EE, Gens A, Josa A (1990) A constitutive model for partially saturated soils. Géotechnique 40(3):405–430
2. Anders G, Radhakrishna H (1988) Computation of temperature field and moisture content in the vicinity of current carrying underground power cables. In: IEE proceedings C (generation, transmission and distribution), vol. 135, IET, pp 51–62
3. Bishop AW (1960) The principles of effective stress. Norges Geotekniske Institutt, Trondheim
4. Bishop AW, Blight G (1963) Some aspects of effective stress in saturated and partly saturated soils. Géotechnique 13(3):177–197
5. Bolzon G, Schrefler BA (2005) Thermal effects in partially saturated soils: a constitutive model. Int J Numer Anal Methods Geomech 29(9):861–877
6. Borja RI (2002) Bifurcation of elastoplastic solids to shear band mode at finite strain. Comput Methods Appl Mech Eng 191(46):5287–5314
7. Borja RI (2004) Cam-clay plasticity, Part V: A mathematical framework for three-phase deformation and strain localization analyses of partially saturated porous media. Comput Methods Appl Mech Eng 193:5301–5338
8. Borja RI (2013) Plasticity modeling & computation. Springer, Berlin
9. Borja RI, Song X, Wu W (2013) Critical state plasticity. Part VII: Triggering a shear band in variably saturated porous media. Comput Methods Appl Mech Eng 261–262:66–82
10. Borja RI, Tamagnini C (1998) Cam-clay plasticity. Part III: Extension of the infinitesimal model to include finite strains. Comput Methods Appl Mech Eng 155(1):73–95
11. Borja RI, Tamagnini C, Amorosi A (1997) Coupling plasticity and energy-conserving elasticity models for clays. J Geotech Geoenviron Eng 123(10):948–957
12. Buscarnera G, Nova R (2011) Modelling instabilities in triaxial testing on unsaturated soil specimens. Int J Numer Anal Methods Geomech 35(2):179–200
13. Callari C, Armero F, Abati A (2010) Strong discontinuities in partially saturated poroplastic solids. Comput Methods Appl Mech Eng 199(23):1513–1535
14. Coussy O (2004) Poromechanics. Wiley, Hoboken
15. De Boer R (2000) Theory of porous media: highlights in historical development and current state. Springer, New York
16. De Borst R, Sluys L, Muhlhaus HB, Pamin J (1993) Fundamental issues in finite element analyses of localization of deformation. Eng Comput 10(2):99–121
17. Dumont M, Taibi S, Fleureau JM, Abou-Bekr N, Saouab A (2011) A thermo-hydro-mechanical model for unsaturated soils based on the effective stress concept. Int J Numer Anal Methods Geomech 35(12):1299–1317
18. Dusseault MB, Wang Y, Simmons J (1988) Induced stresses near a fire flood front. AOSTRa J Res 4:153–170
19. Duszek MK, Perzyna P (1991) The localization of plastic deformation in thermoplastic solids. Int J Solids Struct 27(11):1419–1443
20. Ehlers W, Graf T, Ammann M (2004) Deformation and localization analysis of partially saturated soil. Computer Methods Appl Mech Eng 193(27):2885–2910
21. François B, Laloui L (2008) Acmeg-ts: a constitutive model for unsaturated soils under non-isothermal conditions. Int J Numer Anal Method Geomech 32(16):1955–1988
22. Fredlund DG (2006) Unsaturated soil mechanics in engineering practice. J Geotech Geoenviron Eng 132(3):286–321
23. Fredlund DG, Xing A (1994) Equations for the soil-water characteristic curve. Can Geotech J 31(4):521–532
24. Gallipoli D, Gens A, Sharma R, Vaunat J (2003) An elasto-plastic model for unsaturated soil incorporating the effects of suction and degree of saturation on mechanical behaviour. Géotechnique 53(1):123–136
25. Gens A (1995) Constitutive laws. Springer, New York
26. Gens A (2010) Soil-environment interactions in geotechnical engineering. Géotechnique 60(1):3–74
27. Grant SA, Salehzadeh A (1996) Calculation of temperature effects on wetting coefficients of porous solids and their capillary pressure functions. Water Resour Res 32(2):261–270
28. Hill R (1962) Acceleration waves in solids. J Mech Phys Solids 10(1):1–16
29. Hueckel T, Borsetto M (1990) Thermoplasticity of saturated soils and shales: constitutive equations. J Geotech Eng 116(12):1765–1777
30. Jefferies M (1993) Nor-sand: a simple critical state model for sand. Geotechnique 43(1):91–103
31. Khalili N, Geiser F, Blight G (2004) Effective stress in unsaturated soils: review with new evidence. Int J Geomech 4(2):115–126
32. Laloui L, François B (2009) Acmeg-t: soil thermoplasticity model. J Eng Mech 135(9):932–944
33. Laloui L, Nuth M, Vulliet L (2006) Experimental and numerical investigations of the behaviour of a heat exchanger pile. Int J Numer Anal Methods Geomech 30(8):763–781
34. Lu N, Likos WJ (2006) Suction stress characteristic curve for unsaturated soil. J Geotech Geoenviron Eng 132(2):131–142
35. Mašín D, Khalili N (2012) A thermo-mechanical model for variably saturated soils based on hypoplasticity. Int J Numer Anal Methods Geomech 36(12):1461–1485
36. Mitchell JK, Abdel-hadi ON (1979) Temperature distributions around buried cables. IEEE Trans Power Appar Syst 4:1158–1166
37. Nikooee E, Habibagahi G, Hassanizadeh SM, Ghahramani A (2013) Effective stress in unsaturated soils: a thermodynamic approach based on the interfacial energy and hydromechanical coupling. Transport Porous Media 96(2):369–396
38. Nuth M, Laloui L (2008) Effective stress concept in unsaturated soils: clarification and validation of a unified framework. Int J Numer Anal Methods Geomech 32(7):771–801
39. Perić D, Zhao G, Khalili N (2014) Strain localization in unsaturated elastic-plastic materials subjected to plane strain compression. J Eng Mech 140(7):1–12
40. Rice J, Rudnicki J (1980) A note on some features of the theory of localization of deformation. Int J Solids Struct 16(7):597–605
41. Romero E, Gens A, Lloret A (2001) Temperature effects on the hydraulic behaviour of an unsaturated clay. Geotech Geol Eng 19(3–4):311–332
42. Romero E, Gens A, Lloret A (2003) Suction effects on a compacted clay under non-isothermal conditions. Géotechnique 53(1):65–81
43. Rudnicki JW, Rice J (1975) Conditions for the localization of deformation in pressure-sensitive dilatant materials. J Mech Phys Solids 23(6):371–394

44. Salager S, El Youssoufi MS, Saix C (2010) Definition and experimental determination of a soil-water retention surface. Can Geotech J 47(6):609–622
45. Salager S, El Youssoufi MS, Saix C (2010) Effect of temperature on water retention phenomena in deformable soils: theoretical and experimental aspects. Eur J Soil Sci 61(1):97–107
46. Salager S, Francois B, Youssoufi ME, Laloui L, Saix C (2008) Experimental investigations of temperature and suction effects on compressibility and pre-consolidation pressure of a sandy silt. Soils Found 48(4):453–466
47. Salager S, Rizzi M, Laloui L (2011) An innovative device for determining the soil water retention curve under high suction at different temperatures. Acta Geotechnica 6(3):135–142
48. Schiava R, Etse G (2006) Constitutive modeling and discontinuous bifurcation assessment in unsaturated soils. J Appl Mech 73(6):1039–1044
49. Schrefler B (1984) The finite element method in soil consolidation. Ph.D. thesis, University College of Swansea
50. Semnani SJ, White JA, Borja RI (2016) Thermoplasticity and strain localization in transversely isotropic materials based on anisotropic critical state plasticity. Int J Numer Anal Methods Geomech 40(18):2423–2449
51. Simo JC, Hughes TJ (1999) Computational inelasticity, vol 7. Springer, New York
52. Song X (2014) Strain localization in unsaturated porous media. Ph.D. thesis, Stanford University
53. Song X (2017) Transient bifurcation condition of partially saturated porous media at finite strain. Int J Numer Anal Methods Geomech 41(1):135–156
54. Song X, Borja RI (2014) Finite deformation and fluid flow in unsaturated soils with random heterogeneity. Vadose Zone J 13(5):1–11
55. Song X, Borja RI (2014) Mathematical framework for unsaturated flow in the finite deformation range. Int J Numer Methods Eng 97(9):658–682
56. Song X, Borja RI (2015) A meso-scale thermal plasticity model for unsaturated soils and its numerical implementation. ASCE EMI abstract, Stanford University
57. Song X, Borja RI, Wu W (2013) Triggering a shear band in variably saturated porous materials. In: Poromechanics V@ sProceedings of the fifth biot conference on poromechanics, pp 367–370, ASCE
58. Song X, Idinger G, Borja RI, Wu W (2012) Finite element simulation of strain localization in unsaturated soils. In: Unsaturated soils: research and applications, pp. 189–195, Springer
59. Uchaipichat A, Khalili N (2009) Experimental investigation of thermo-hydro-mechanical behaviour of an unsaturated silt. Geotechnique 59(4):339–353
60. Van Genuchten MT (1980) A closed-form equation for predicting the hydraulic conductivity of unsaturated soils. Soil Sci Soc Am J 44(5):892–898
61. Vardoulakis I (1985) Stability and bifurcation of undrained, plane rectilinear deformations on water-saturated granular soils. Int J Numer Anal Methods Geomech 9(5):399–414
62. Vardoulakis I (1996) Deformation of water-saturated sand: I. uniform undrained deformation and shear banding. Géotechnique 46(3):441–456
63. Wu W, Li X, Charlier R, Collin F (2004) A thermo-hydro-mechanical constitutive model and its numerical modelling for unsaturated soils. Comput Geotech 31(2):155–167